# A small angle x-ray scattering study of the droplet–cylinder transition in oil-rich sodium bis(2-ethylhexyl) sulfosuccinate microemulsions

D. I. Svergun, P. V. Konarev, V. V. Volkov, M. H. J. Koch, W. F. C. Sager, J. Smeets, and E. M. Blokhuis

Citation: J. Chem. Phys. **113**, 1651 (2000); doi: 10.1063/1.481954
View online: https://doi.org/10.1063/1.481954
View Table of Contents: http://aip.scitation.org/toc/jcp/113/4
Published by the American Institute of Physics

# A small angle x-ray scattering study of the droplet–cylinder transition in oil-rich sodium bis(2-ethylhexyl) sulfosuccinate microemulsions

D. I. Svergun
*European Molecular Biology Laboratory, EMBL c/o DESY, Notkestraße 85, D-22603 Hamburg, Germany and Institute of Crystallography, Russian Academy of Sciences, Leninsky, prospect 59, 117333 Moscow, Russia*

P. V. Konarev and V. V. Volkov
*Institute of Crystallography, Russian Academy of Sciences, Leninsky prospect 59, 117333 Moscow, Russia*

M. H. J. Koch
*European Molecular Biology Laboratory, EMBL c/o DESY, Notkestraße 85, D-22603, Hamburg, Germany*

W. F. C. Sager
*Faculty of Chemical Technology, Membrane Technology, University of Twente, 7500 AE, Enschede, The Netherlands*

J. Smeets and E. M. Blokhuis
*Colloid and Interface Science, Leiden Institute of Chemistry, Gorlaeus Laboratories, P.O. Box 9502, 2300 RA Leiden, The Netherlands*

(Received 29 September 1999; accepted 26 April 2000)

A method for nonlinear fitting of x-ray scattering data from polydisperse mixtures was developed. It was applied to the analysis of the structural changes in the droplet phase of oil-rich water-in-oil (w/o) sodium bis(2-ethylhexyl) sulfosuccinate (AOT) microemulsions with increasing temperature or upon addition of salt. Data were collected at different temperatures (15 to 60 °C) and salt concentrations (up to 0.6% NaCl) within the one-phase region of the $L_2$ phase (w/o microemulsion) for different droplet sizes (water/AOT molar ratio $w_o = 25$ to 56) and concentrations (droplet weight fraction $c_w = 2\%$ to 20%). This allowed us to distinguish between contributions from individual scattering particles, e.g., droplets and cylinders to the total scattering intensity. The complete data set containing over 500 scattering curves could be interpreted by fitting the scattering of weighted sums of AOT covered water droplets, long cylinders, and inverse AOT micelles containing bound water only, to the experimental scattering curves. The polydispersity of the droplets and cylinders is described by Schulz distributions and the interactions between the droplets are calculated using a sticky hard-sphere potential in the Percus–Yevick approximation. The volume fractions of the components, their average sizes and polydispersity, and the stickiness of the water/AOT droplets are determined by a nonlinear fit to the experimental data. © *2000 American Institute of Physics*. [S0021-9606(00)50528-5]

## I. INTRODUCTION

Over the past three decades, it has been shown that microemulsions are structurally well-defined, self-organized mixtures of water (or salt solutions), oil, and surfactant(s) that can form a variety of thermodynamically stable phases. These comprise droplet phases of water droplets in oil (w/o microemulsion or $L_2$ phase) or oil droplets in water (o/w or $L_1$ phase), both surrounded by a monomolecular surfactant layer, as well as bicontinuous mono- and bilayer phases. The latter consists of a network of water and/or oil channels separated by a continuous surfactant mono- or bilayer film. If the temperature and/or the ionic strength of the aqueous phase are varied, a rich phase behavior is generally revealed,[1–6] whereby microemulsion phases can coexist with water and/or oil excess phases as well as liquid crystalline phases, forming two- and three-phase equilibria. The global features of the phase behavior, including the formation of liquid crystalline phases, have been attributed to changes in the interfacial surfactant layer and described using the curvature energy concept introduced by Helfrich[7] in terms of rigidity constants and spontaneous curvature.[8–10] There is, however, still no all-embracing picture nor complete understanding of the structural evolution of the transition of droplets to bicontinuous phases including droplet aggregation and the formation of cylinders.

There is ample experimental evidence from, e.g., dielectric spectroscopy, electro-optic birefringence (Kerr effect), fluorescence quenching, turbidity, and temperature jump experiments, for droplet aggregation within the existence regions of $L_1$ and $L_2$ phases. Aggregation phenomena have been observed, e.g., with increasing temperature in ionic w/o microemulsions such as the AOT [sodium bis(2-ethylhexyl) sulfosuccinate] system as well as nonionic o/w microemulsions.[11–14] Conductivity measurements have also attracted considerable interest, especially for w/o AOT microemulsions for which a jump in conductivity over 2–3 orders of magnitude has been reported following an increase in the temperature or in the amount of the internal phase.[15–19]

 

Although a number of conductivity studies were devoted to the investigation of the influence of different oils, of additives such as alcohols, and different salt concentrations of the internal phase, the mechanism of the actual charge transfer has not been elucidated. It is still a matter of debate whether the increase in conductivity can be explained solely by charge transfer between clustered droplets (hopping mechanism) or by an opening into water channels, assuming that the formation of channels and bicontinuous structures is necessary to explain the high conductivities. Bicontinuous microemulsion phases that generally form at comparable amounts of water and oil were found in the AOT system only upon addition of salt.[20]

The results of small angle x-ray (SAXS) and neutron (SANS) scattering studies on the $L_1$ and $L_2$ microemulsion phases at low content of dispersed phase have so far been interpreted mainly within the framework of liquid state theories. The microemulsion droplets have been characterized with respect to their size, polydispersity, form fluctuations, and interaction parameters. The linear dependence of the droplet size on the molar internal phase/surfactant ratio, e.g., water/surfactant for AOT microemulsions, has been established. Average droplet radii have been determined in the range of 3 to 20 nm, and their populations display a moderate (about 20%) size polydispersity.[21–26] Increasing interactions between the droplets, observed upon raising the temperature, have been described using Baxter's model by introducing a temperature-dependent stickiness parameter in the hard-sphere potential, leading to a liquid–gas phase transition at higher temperatures.[27–29] Only recently has (the onset of) droplet aggregation been addressed theoretically within the framework of the Helfrich free energy.[30–32]

Increase in scattering at low angles has been attributed to critical scattering within the Ornstein–Zernike theory. The water/AOT/decane systems display a lower critical point at a molar water/surfactant ratio $w_o$ of 40.8 at a temperature of 40 °C and a droplet volume fraction of 10%.[33–35] Recently, Ilgenfritz *et al.*[36] analyzed the increase in scattering at very low angles in nonionic w/o microemulsions with decreasing temperature using a structure factor for fractal aggregation, but the fits obtained were significantly worse than those resulting from applying the Ornstein–Zernike structure factor. Evidence for the formation of cylinders at low water/AOT ratios has been found by small-angle scattering for w/o microemulsions stabilized by bis(2-ethylhexyl) sulfosuccinate with bi- or trivalent counterions rather than sodium ions used in the present investigation.[37–39] Glatter *et al.*[40,41] found cylindrical structures at high temperatures in the $L_1$ phase of nonionic microemulsions. In all the above papers, the data analysis has been restricted to limiting cases of systems assumed to contain only one type of scatterer, e.g., spherical, cylindrical, or lamellar structures.

At high dispersed phase contents and within the bicontinuous region of the phase diagram, a distinct peak is observed in the scattering curve. This microemulsion peak has been first analyzed using a sticky hard-sphere potential for the droplet structure factor.[29] A more consistent interpretation is given in terms of Landau–Ginsburg-based theories[42] or using the disordered open connected cell model introduced by Ninham and co-workers.[43]

SAXS and SANS are the most appropriate techniques for studying structural transitions on the length scale involved in microemulsion systems. One of the reasons that no quantitative analysis of the sphere-to-cylinder transition occurring in microemulsion droplet phases (e.g., by increasing temperature for the AOT systems) is yet available certainly lies in the difficulty of analyzing scattering data of nonuniform particle mixtures. The distributions of components—spheres and cylinders, in this case—are characterized by more than one parameter, e.g., radius, polydispersity, length, and volume fractions. This leads to a complex numerical data analysis problem involving a large number of parameters and requiring a large set of experimental data. In the present study, samples were measured for each droplet size and concentration in a range of temperatures lying between the lower and the upper phase boundary. This allows to establish systematic trends and detect and rule out inconsistencies. Data were always taken from the lower phase boundary, the solubilization limit,[44] below which water is expelled and the $L_2$ phase is in equilibrium with an excess water phase ($L_2+W$), or from 15 °C onward if $T_{L2+W\rightarrow L2}<15\,^{\circ}\mathrm{C}$ up to the upper phase boundary ($2\phi$) or up to 60 °C if $T_{L2\rightarrow 2\phi}>60\,^{\circ}\mathrm{C}$. Above the upper phase boundary of the $L_2$ phase and depending on the $w_o$ value, either two oil-continuous microemulsion phases or a lamellar phase in equilibrium with an almost pure oil phase ($L_\alpha+L_2$) forms. In this way it was possible to capture samples consisting of droplets only (low temperatures) and of mixtures of spheres and cylinders with a high fraction of cylinders (high temperatures). The AOT system was chosen because its $L_2$ phase can be studied over a wide range of droplet size, droplet concentration, temperatures, and salt content of the internal phase without addition of a cosurfactant, e.g., alcohol. Addition of alcohol, necessary to obtain $L_2$ phases with other ionic surfactants like sodium dodecyl sulfate (SDS), would have complicated the analysis.[45] Moreover, the AOT system is one of the most studied (ionic) microemulsion systems and often used to test liquid state theories[29] and for determining properties of the interfacial surfactant layer,[46–52] which provides a solid base for the present investigation.

In the present paper, the method developed to analyze scattering data from mixtures of spheres and cylinders will be described in detail. This method is more generally valid and allows us to analyze the scattering data for systems containing different types of particles, taking into account polydispersity and interparticle interaction effects. Its application is illustrated by the quantitative characterization of the droplet–cylinder transition in AOT–water–isooctane and AOT–water–decane microemulsions. In a forthcoming paper, the results on the structural transition in AOT microemulsions will be discussed in the framework of the Helfrich free energy.

## II. THEORY

### A. Scattering from a mixture

The scattering intensity from a mixture of different types of noninteracting components can be represented as a linear

combination of the partial intensities from the components weighted by their volume fractions. If the partial intensities are known, the volume fractions are readily evaluated by a linear least-squares fit of the scattering intensity from the mixture. This approach is useful, e.g., to analyze the oligomeric composition of protein mixtures.[53] If the scattering particles have defined shapes but differ in size and polydispersity, these characteristics can be parametrized and restored along with their volume fractions using a nonlinear fitting procedure. The equations for the latter case are derived below.

Let us consider a system consisting of $K$ noninteracting components and describe the polydispersity of a $k$th component by a size distribution function $N_k(R)$ corresponding to the number of particles with characteristic size $R$. The scattering intensity from the $k$th component is an isotropic function depending on the momentum transfer $s=(4\pi/\lambda)\sin\theta$ ($\lambda$ is the wavelength, and $2\theta$ is the scattering angle) that can be written as

$$I_k(s)=\int_0^\infty N_k(R)[v_k(R)\Delta\rho_k(R)]^2 i_{0k}(s,R)dR, \tag{1}$$

where $\Delta\rho_k(R)$, $v_k(R)$, and $i_{0k}(s,R)$ denote the contrast, volume, and normalized scattering intensity (form factor) of the particle with size $R$ [these functions are defined by the shape and internal structure of the particles, and $i_{0k}(0,R)=1$]. The total volume of the component is given by

$$V_k=\int_0^\infty v_k(R)N_k(R)dR, \tag{2}$$

so that Eq. (1) can be rewritten as

$$I_k(s)=V_k\frac{\int_0^\infty D_k(R)v_k(R)[\Delta\rho_k(R)]^2 i_{0k}(s,R)dR}{\int_0^\infty D_k(R)dR}, \tag{3}$$

where $D_k(R)=N_k(R)v_k(R)$ denotes the volume distribution function, which, as seen from Eq. (3), can without loss of generality be normalized, $\int_0^\infty D_k(R)dR=1$. The scattering intensity from the mixture is written as a linear combination of the partial intensities

$$I(s)=\sum_{k=1}^{K} V_k I_{k0}(s), \tag{4}$$

where

$$I_{k0}(s)=\int_0^\infty D_k(R)v_k(R)[\Delta\rho_k(R)]^2 i_{0k}(s,R)dR. \tag{5}$$

The volume distribution functions $D_k(R)$ can be conveniently represented by a normalized Schulz distribution[54] using two parameters, an average value $R_{0k}$ and a dispersion $\Delta R_k$

$$D_k(R)=G(R,R_{0k},\Delta R_k)=\left(\frac{z+1}{R_{0k}}\right)^{z+1}\frac{R^z}{\Gamma(z+I)}\exp\left[-\frac{(z+1)R}{R_{0k}}\right], \tag{6}$$

where $z=(R_{0k}/\Delta R_k)^2-1$.

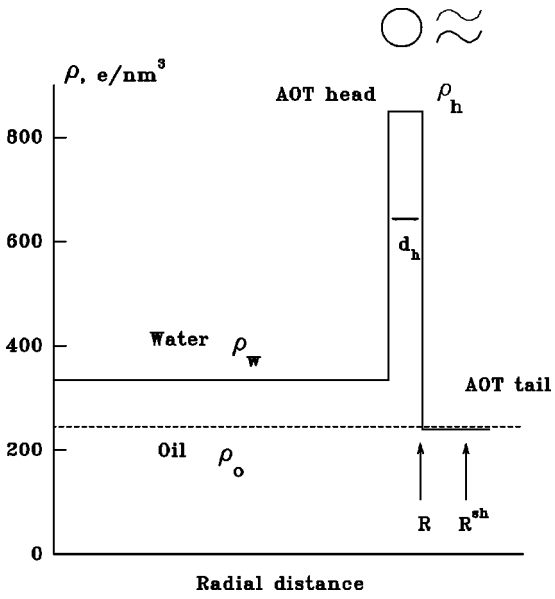


FIG. 1. Radial electron density profile of an AOT microemulsion droplet. For explanations, see the text.

### B. Interference effects

In Eqs. (1) and (4), interparticle interference effects were neglected, which is only valid at low particle concentrations. As no analytical expression exists for the scattering from a mixture of interacting particles of different shapes in the general case, simplifying assumptions have to be made. In the following, only interactions between the particles belonging to the same component will be considered, and the partial intensities will be taken in the form

$$J_{k0}(s)=I_{k0}(s)S_k(s), \tag{7}$$

where $S_k(s)$ is the structure factor describing the interference effects for the $k$th component.

### C. Particle structure and interaction potential

To define the functions $\Delta\rho_k(R)$, $v_k(R)$ and $i_{0k}(s,R)$ and $S_k(s)$, *a priori* knowledge about the shape, internal structure, and interaction potentials between the particles in the components of the mixture is required. The water droplets in water/oil microemulsions are surrounded by the AOT molecules and the radial electron density distribution profile of a droplet can be represented[26] by a step function as illustrated in Fig. 1. The inner part of a droplet is occupied by water (electron density $\rho_w=334\,e/\mathrm{nm}^3$) and the high density ($\rho_h\approx 850\,e/\mathrm{nm}^3$) region corresponds to the polar AOT headgroups. The outer shell of the AOT hydrocarbon tails has a density close to that of oil ($\rho_t\approx\rho_o\approx 240\,e/\mathrm{nm}^3$) and does not contribute to the scattering. The form factor of the droplet is defined by the ratio $\delta=d_h/R$ of the headgroup size $d_h$ to the droplet radius $R$ and by the ratio of the contrasts $\xi=\Delta\rho_2/\Delta\rho_1=(\rho_h-\rho_o)/(\rho_w-\rho_o)$. The profile in Fig. 1 was used to describe the radial density distribution inside the water droplets and the reversed AOT micelles, and also that perpendicular to the long axis of the cylindrical particles. The contrast of the particle is expressed as

$$\Delta\rho_k(R)=\Delta\rho_1[\xi-(1-\xi)(1-\delta)^p], \tag{8}$$

where the exponent $p$ is equal to 3 for a droplet and 2 for a cylinder. As noted in Refs. 27 and 28, if $R\gg d_h$, the results are not sensitive to the individual values of $d_h$ and $\xi$ provided their product remains constant. In the following, the values used for $d_h=0.2$ nm and $\xi=6$ were estimated from the chemical composition of the AOT molecule. The expressions for the form factors of spherical and cylindrical particles are given in several textbooks, e.g., in Ref. 55.

For spherically symmetric interaction potentials, the structure factor can be calculated in the Perkus–Yevick approximation.[56] Following Robertus,[27,28] we used the sticky hard-sphere potential introduced by Baxter[57]

$$S_k(s,R_k^{\rm hs},\eta_k,\tau_k)=[A^2(s,R_k^{\rm hs},\eta_k,\tau_k)+B^2(s,R_k^{\rm hs},\eta_k,\tau_k)]^{-1}, \tag{9}$$

where $R^{\rm hs}$ is the hard-sphere interaction radius, $\eta$ the hard-sphere volume fraction, and $\tau$ the stickiness parameter that determines the magnitude of the attractive potential at the surface (the expressions for $A$ and $B$ are given by Baxter[57]). The contribution of the hydrocarbon tails of AOT which was neglected when calculating the particle scattering must be taken into account here as it increases both the radius of the hard spheres ($R^{\rm hs}=R+d_t$, where $d_t$ is the apparent width of the layer of AOT tails) and their volume fraction.

### D. Nonlinear fitting

Using the above parametrization, the scattering intensity from a mixture is written as

$$I(s)=\text{const}\sum_{k=1}^{K}\varphi_k I_{k0}(s,R_{0k},\Delta R_k)S_k(s,R_k^{\rm hs},\eta_k,\tau_k), \tag{10}$$

where $\varphi_k=V_k/\Sigma V_k$ are the volume fractions of the components. To determine the volume fractions and other parameters characterizing the mixture, the experimental scattering intensity $I_{\rm exp}(s)$ should be decomposed into the partial functions (10). This can be done by a nonlinear minimization of the residual

$$\chi^2=\sum_{j=1}^{N}\{[cI(s_j)-I_{\rm exp}(s_j)]/\sigma(s_j)\}^2, \tag{11}$$

where $N$ is the number of experimental points and $\sigma(s)$ denotes the statistical error. The use of the scale factor

$$c=\sum_{j=1}^{N}I(s_j)I_{\rm exp}(s_j)/\sigma^2(s_j)\Big/\sum_{j=1}^{N}\{[I(s_j)/\sigma(s_j)]\}^2, \tag{12}$$

allows us to fit the experimental data on a relative scale.

The minimization was performed using the multivariant optimization program package OPTIS (Volkov, unpublished). As the ranges of the parameters in Eq. (10) can be predicted *a priori*, the Broyden–Fletcher–Goldfarb–Shanno method with simple bounds on the problem variables (EO4JAF algorithm[58]) was chosen to minimize the residual (11).

Due to the nonlinearity of the fitting procedure, the error estimates in the parameters extracted from the data cannot be directly obtained. For many samples, repeated measurements were performed in the same conditions, and this allowed us to estimate the propagated errors in the fitting parameters by averaging the results of these independent fits. In all cases, the absolute errors in the volume fractions did not exceed 0.04; those in the radii of spheres and cylinders were less than 0.1 and 0.2 nm, respectively. The determination of the stickiness parameter $\tau$ was the least accurate, leading to relative errors of up to 20%.

## III. EXPERIMENT

### A. Sample preparation

Sodium bis(2-ethylhexyl) sulfosuccinate (AOT) was obtained from Fluka (98% purum) and purified by extractions with water and methanol as described elsewhere.[59] Isooctane (per analysis, Merck) and decane (purum, Fluka) were used without further purification and NaCl was of the highest commercially available purity. Microemulsions samples were prepared by weighing in appropriate amounts of surfactant, oil, and water (or salt solution). The samples are characterized by the water to surfactant molar ratio ($w_o$) and the weight fraction of droplets $c_w$ expressed as

$$w_o=\frac{(m_{\rm W}+fm_{\rm AOT})M({\rm AOT})}{(1-f)m_{\rm AOT}M({\rm H_2O})},$$

and

$$c_w=\frac{m_{\rm W}+m_{\rm AOT}}{m_{\rm W}+m_{\rm AOT}+m_{\rm O}},$$

where $m_{\rm AOT}$, $m_{\rm O}$, and $m_{\rm W}$ stand for the masses of AOT, oil, and water (or salt solution), respectively. $M$(AOT) and $M(H_2O)$ correspond to the molecular weight of AOT and water, whereby $M({\rm AOT})=444.56$ g. The factor $f=0.039$ takes into account that each AOT molecule contains approximately one bound water molecule. The salt concentration of the aqueous phase is given by the weight fraction

$$\varepsilon=\frac{m_{\rm NaCl}}{m_{\rm NaCl}+m_{\rm H_2O}}.$$

All samples were measured at temperatures within the one-phase region of the $L_2$ phase (w/o microemulsion). The temperatures ranged from 15 °C (or the lower phase boundary $T_{L2+W\to L2}$ if $T_{L2+W\to L2}>15$ °C) to 60 °C (or the upper phase boundary $T_{L2\to 2\phi}$ if $T_{L2\to 2\phi}<60$ °C). To indicate the existence region of the $L_2$ phase, the phase boundaries for certain $c_w$ values for the water–AOT–isooctane system and at different salt concentrations for the water–AOT–decane system are given in Table I. The phase boundaries depend only slightly on the $c_w$ value.

### B. Scattering experiments and data treatment

The synchrotron radiation x-ray scattering data were collected following standard procedures using the X33 camera[60–62] of the European Molecular Biology Laboratory on the storage ring DORIS III of the Deutsches Elektronen

TABLE I. Existence regions of the $L_2$ phase for the AOT w/o microemulsions.

| $\varepsilon$, wt % | $w_o$ | $c_w$, wt % | $T(L_2+W\rightarrow L_2)$, °C | $T(L_2\rightarrow 2\Phi)$, °C |
|---|---|---|---|---|
| AOT–water–iso-octane[a] | | | | |
| 0 | 25 | 10 | <15 | >80 |
| 0 | 35 | 10 | <15 | 57.5±0.5 |
| 0 | 45 | 10 | <15 | 45.5±0.1 |
| 0 | 56 | 10 | <15 | 29.5±0.3[a] |
| AOT–water–decane | | | | |
| 0 | 36.8 | 30 | <15 | 37.7±0.15 |
| | 50.3 | 35 | <15 | 21.35±0.12[a] |
| 0.2 | 36.8 | 30 | <15 | 47.6±0.2 |
| | 50.3 | 30 | <15 | 37.05±0.25 |
| 0.4 | 36.8 | 30 | <15 | 55.7±0.3 |
| | 50.3 | 30 | 19.7±0.5 | 47.15±0.15 |
| 0.6 | 36.8 | 25 | 20.7±0.3 | 63.6±0.2 |
| | 50.3 | 30 | 29.55±0.25 | 56.95±0.35 |

[a]Transition $L_2\rightarrow L_2+L_\alpha$.

Synchrotron (DESY). At a sample-detector distance of 4 m and a wavelength $\lambda=0.15$ nm, the range of momentum transfer $0.1<s<1.6\,\mathrm{nm}^{-1}$ was covered. The focusing geometry and narrow wavelength bandpass ($\Delta\lambda/\lambda\approx 0.005$) and the use of a linear multiwire proportional detector with delay line readout[63] resulted in negligible smearing effects. The prethermostated samples were injected into a thermostated silver cell with mica windows with a cell volume of 125 $\mu$l and an optical pathlength of 1 mm. The temperature was controlled within ±0.2 °C using a waterbath.

The transmission of all samples was determined by measuring the scattering pattern of a tripalimitin sample placed in front of the cell. The experimentally determined absorption coefficients compared well with values calculated from the absorption coefficients of the elements. The attenuation was found to be proportional to $\exp(c_w)$ independently of the $w_o$ value and the salt concentration used. The detector response was measured using an $Fe^{55}$ source and the geometrical effects were corrected as described elsewhere.[64] In the data processing procedures, using the program SAPOKO (Svergun & Koch, unpublished) which involves statistical error propagation, all scattering patterns were divided by the detector response, multiplied by $\exp(c_w)$, and after subtraction of the corresponding solvent file divided by $c_w$.

To evaluate the distribution functions at the lower and upper ends of the temperature scans, the appropriate integral equations were solved using the indirect transform program GNOM.[65,66] The distance distribution functions $p(r)$ were computed assuming monodisperse systems of particles with arbitrary shape from the transformation

$$I(s)=4\pi\int_0^{D_{\max}} p(r)\frac{\sin sr}{sr}\,dr, \tag{13}$$

where $D_{\max}$ is the maximum diameter of the particle. Evaluation of the volume distribution functions $D(R)$ for polydisperse systems of spherical particles was based on the equation

$$I(s)=\int_{R_{\min}}^{R_{\max}} D(R)v(R)i_0(s,R)\,dR, \tag{14}$$

where $R_{\min}$ and $R_{\max}$ are minimum and maximum radii of the spheres in the system, respectively, and $v(R)$ and $i_0(s,R)$ are the volume and scattering from the particle of size $R$, respectively. The form factors were computed from the radial distribution functions in Fig. 1 for a ratio of contrasts $\xi\cong 6$. Note that Eq. (14) implies that the ratio $\delta=d_h/R$, and not the size of the headgroup itself, remains constant. This simplification is justified to obtain an estimate of the size distribution for moderate polydispersities. The value of $\delta$ for each individual system was taken to be $0.2/R_0$ [nm], where $R_0$ is the average particle radius.

## IV. RESULTS

In this section, selected series of data are presented to illustrate how the model used to analyze the complete data set was developed and further used to analyze the structural changes occurring in the AOT system upon increasing temperature and/or salt concentration.

### A. Selection of the multicomponent model

Initial inspection of the scattering data recorded at different $w_o$ values and salt concentrations of the internal phase with increasing temperature suggests that a transition from spherical droplets to cylindrical or rod-like aggregates takes place. Both the measured scattering curves (see the different temperature series in Fig. 2) as well as the distance distribution functions $p(r)$ obtained using the program GNOM in the monodisperse approximation indicate the continuous formation of relatively long cylindrical structures by a significant increase in scattering at low angles. The first attempt to model the system by a two-component mixture of spherical and cylindrical particles, both described by monomodal size distributions over the radii of spheres and cylinders, yielded poor fits to most of the experimental data sets, especially at higher angles, as illustrated in the two-component model in Fig. 2. Additional calculations were thus made to find a physically meaningful model to fit the data.

The scattering data at low temperatures and low droplet concentrations $c_w$ were first analyzed for polydispersity us-

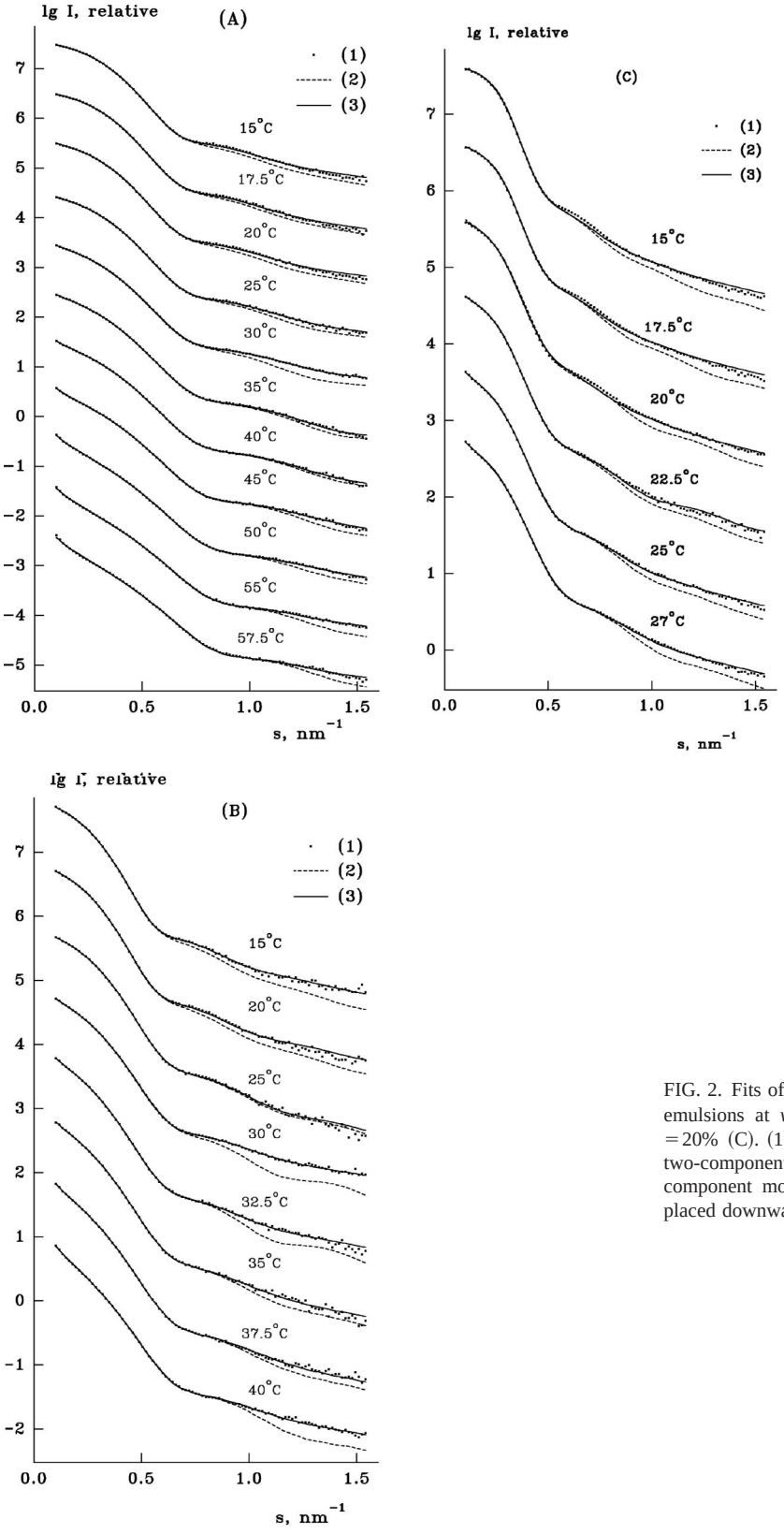


FIG. 2. Fits of the scattering data from the AOT–water–iso-octane microemulsions at $w_o=35$, $c_w=5\%$ (A), $w_o=45$, $c_w=2\%$ (B), $w_o=56$, $c_w=20\%$ (C). (1): Experimental data; (2) and (3): Best fits provided by the two-component model without AOT reverse micelles and by the three-component model, respectively. Successive curves in each plot are displaced downwards by one logarithmic unit for better visualization.

ing the modified version of GNOM described in Sec. III B. Close to the lower phase boundary of the $L_2$ phase ($L_2+W \rightarrow L_2$), microemulsion samples are known to consist of only spherical droplets that behave like hard spheres. Figure 3(A) illustrates the volume distribution functions computed for different AOT microemulsions for different $w_o$ values at $T=15\,^{\circ}\mathrm{C}$. All distributions are bimodal, showing distinct fractions of small (radii about 1 nm) and large (radii from 5 to 15 nm) particles. The sizes of the larger particles vary significantly depending on the $w_o$ ratio, as expected for w/o microemulsion droplets. Moreover, the asymmetric profiles of the modes of the larger fraction can be neatly approximated by

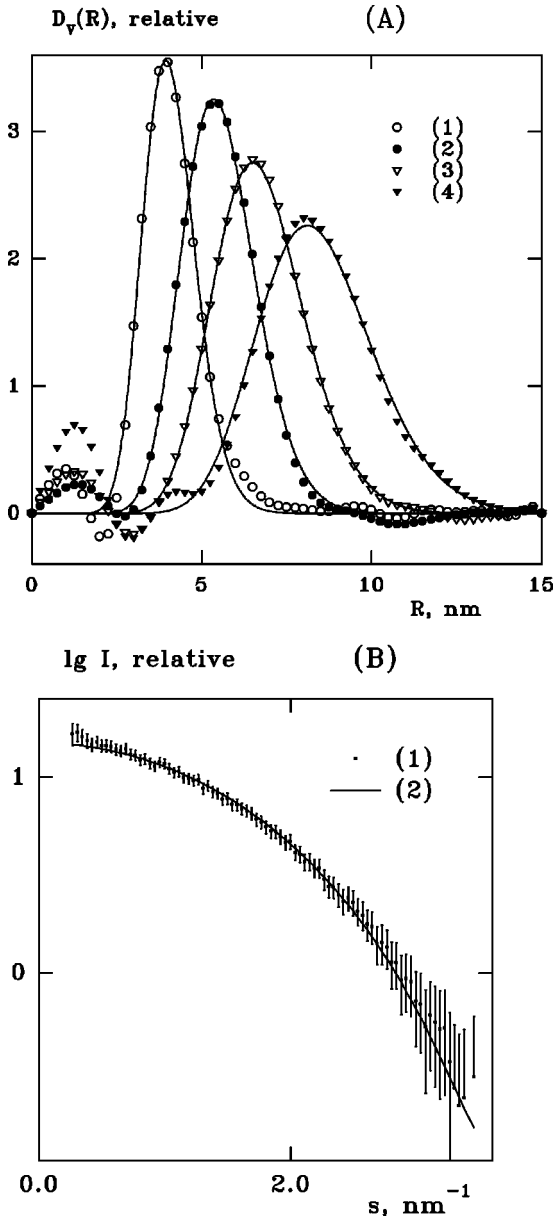


FIG. 3. (A) Computed volume distribution functions for the AOT–water–iso-octane microemulsions at 15 °C for $c_w = 2\%$ (symbols) approximated by Schulz distributions (lines). Distributions (1–4) correspond to $w_o = 25$, 35, 45, and 56, respectively. (B) X-ray scattering from a 2 wt % AOT solution in decane (1) and the scattering computed from the model of an AOT reverse micelle (2).

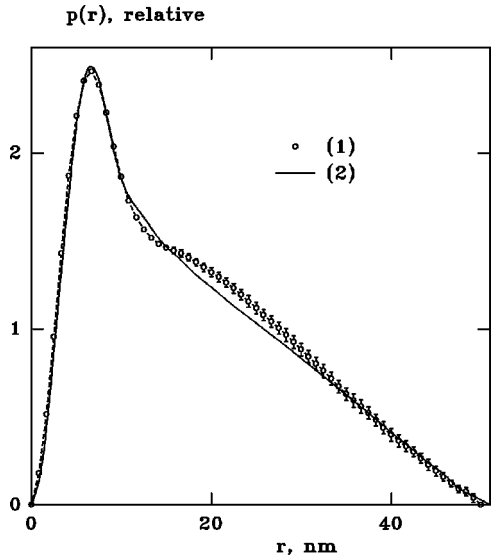


FIG. 4. Distance distribution function computed from the scattering curve of the AOT–water–iso-octane microemulsion ($w_o = 35$, $c_w = 2\%$) at 55 °C (1) and the theoretical function for a cylinder with a radius of 4.5 nm and a length of 50 nm.

Schulz distributions [lines in Fig. 3(A)] which justifies the choice of the latter function to parametrize the polydispersity of the droplets.

In contrast, the small particles have practically the same radius (about 1 nm) at all molar ratios. This size corresponds to that of the reversed micelles of AOT formed in binary AOT–oil systems.[25] The experimental x-ray scattering pattern from a binary AOT–decane system without water shown in Fig. 3(B) can be neatly fitted by the scattering from the model in Fig. 1 with an outer radius $R = 1$ nm. This suggests that even ternary AOT–water–oil microemulsions contain a small part of the AOT molecules in the form of reverse micelles containing only the water molecules bound to the AOT heads. Accounting for the reverse micelles improves the fits to the SAXS curves significantly as already reported by North *et al.*[67] Due to the high shell contrast of the AOT micelles with respect to oil and the negligible incoherent scattering in SAXS, a small volume fraction of reverse micelles can be detected more easily with this technique than with SANS. The component consisting of the reverse micelles was taken into account in subsequent data analysis.

To analyze the shape of the surfactant aggregates formed at high temperatures, corresponding scattering curves were first treated as monodisperse systems using GNOM. Figure 4 presents the distance distribution function evaluated for a microemulsion with $w_o = 35$ at $T = 55\,°\mathrm{C}$ and $c_w = 5\%$ along with the theoretical $p(r)$ of a cylinder with length $L = 50$ nm and radius $R_c = 4.5$ nm. The two distributions agree well, indicating that the scattering from the system is largely determined by cylinder-like particles (although, as it will be demonstrated below, the droplets never disappear entirely). The length of the cylinder cannot be accurately deduced from the scattering data because of the cutoff at small angles ($s_{\min} = 0.1\,\mathrm{nm}^{-1}$). The maximum size of 50 nm was the largest one allowing us to reliably compute the $p(r)$ functions using GNOM, but the existence of longer particles cannot be excluded. A further increase of $L$ would, however, not change the shape of the scattering curve of a cylindrical particle in the experimental range (the differences would come at smaller momentum transfer values), so that the results presented below are also valid if longer cylinders are formed. For simplicity, the length polydispersity of the cylinders was neglected. Spherical particles are expected to grow into elongated ones according to an exponentially decaying function.[68–70] For cylinders with an average length of, say, 20 nm the contribution of the short cylinders can be assumed not to influence the scattering curves in a significant way.

Based on the above, the following three-component model was selected to describe the scattering from the AOT water-in-oil microemulsions:

TABLE II. Parameters used to describe the AOT microemulsions.

| Component | Parameters | Minimum value | Maximum value |
|---|---|---|---|
| Component 1: Spherical droplets | Volume fraction $\varphi_1$ | 0 | 1 |
| | Average radius $R_{01}$ | 4 nm | 10 nm |
| | Dispersion $\Delta R_1$ | 0.1 nm | 3 nm |
| | Stickiness $\tau$ | 0.1 | 100 |
| Component 2: Cylinders of fixed length $L=50$ nm | Volume fraction $\varphi_2$ | 0 | 1 |
| | Average radius $R_{02}$ | 3 nm | 9 nm |
| | Dispersion $\Delta R_2$ | 0.1 nm | 1 nm |
| Component 3: AOT reverse micelles, radius $R_3=1.0$ nm | Volume fraction $\varphi_3$ | 0 | 1 |

(i) spherical particles (water/AOT droplets) with sticky hard-sphere interaction potential and polydispersity described by a Schulz distribution;
(ii) long cylinders (cylindrical AOT/water aggregates) with fixed length and polydispersity of radius described by the Schulz distribution.
(iii) small spherical particles with fixed radius (reverse micelles of AOT).

Table II presents the parameters used to fit the experimental data along with their lower and upper boundaries. All volume fractions $\varphi_k$ should be in the range [0,1] by definition; the stickiness is allowed to range from $\tau=0.1$ (highly sticky potential at the validity limit of Baxter's approximation) to 100 (hard-sphere potential). The boundaries for the radii of droplets and cylinders were selected from physical considerations. The apparent width of the layer of AOT tails was fixed at $d_t=0.4$ nm, and the volume fraction of the hard spheres in the system computed as $\eta_1=c_1(\rho_o/\rho_w)[(R_{01}+d_t)/R_{01}]^3$. The radius of the AOT reverse micelles was fixed at $R_3=1$ nm.

### B. Temperature and concentration dependence

Figure 2 illustrates the fits to the experimental data obtained for several temperature series at different water/AOT molar ratios and droplet concentrations. Accounting for the third component (AOT reverse micelles) significantly improves the fit to the data compared to the two-component model. Using the three-component model, it was possible to fit almost all of the more than 500 independent data sets with a discrepancy $\chi\leqslant 1$. The worst fits with $\chi=1.8$ were observed for curves of the $w_o=56$ system at low temperatures [Fig. 2(C)] and they display only minor systematic deviations from the experimental data.

The typical behavior of the volume fractions and particle sizes as functions of temperature is illustrated in Figs. 5 and 6 for the AOT–water–iso-octane system at $w_o=25$ and 45, respectively, for droplet fractions ranging from 2% to 20%. In all cases, the fraction of spherical droplets decreases, whereas that of the cylinders increases with temperature. Simultaneously, the average radii of both droplets and cylinders decrease, whereby the latter amounts to about 0.7–0.8 of the former. The polydispersity of the water droplets (the ratio $\Delta R_1/R_{01}$) was about 20% and that of the cylinder fraction typically less than 10%. For $w_o=25$ the $L_2$ phase expands over a large temperature range, so that both boundaries are far below and above 15 and 55 °C, respectively. The spherical microemulsion droplets comprise the major fraction at all temperatures. Cylinders start to form above 40 °C and the reversed micelles disappear at temperatures above 45 °C. Neither crossing of the spheres and cylinder curves nor significant dependence on the droplet fraction are observed. The average radii for spheres and cylinders start at 4 and 3 nm, respectively. At a higher $w_o=45$ value, the upper phase boundary is shifted down and the $L_2\rightarrow 2\phi$ transitions lies at about 43 °C, whereby two oil continuous phases form, one rich and the other poor in water and AOT. A crossing between the sphere and the cylinder curve is observed for all $c_w$ values measured. The cylinders are formed much faster and constitute the major fraction of the microemulsion already at 40 °C, whereas the fraction of AOT reverse micelles is nearly constant. The microemulsion at $w_o=45$ displays a small but noticeable concentration dependence: at lower water concentrations (2% to 10%), the volume fraction of spheres and their average size decrease more rapidly with temperature than at higher concentrations (15% to 20%). The crossing between the curves of the spheres and cylinders is clearly shifted to higher temperatures with increasing concentrations, indicating that cylinder formation is reduced at higher concentrations. The average radii for spheres and cylinders start at 7 and 6.2 nm, respectively.

### C. Interactions between water droplets

The importance of accounting for interparticle interactions is illustrated in Fig. 7 presenting the best fits for the $w_o=25$ system for $c_w=20$ wt % using the three-component model. The fits obtained without the interference terms $S_k(s)$ display clear systematic deviations from the experimental data, especially at low temperatures (when the microemulsions consist largely of droplets). From 40 °C onwards, when cylindrical structures start to form [see Fig. 5(a), bottom], the difference between the two fits becomes very small. This sustains the assumption made in the selection of the three-component model taking only droplet–droplet interactions into account. The implementation of the sticky hard-sphere potential described in Sec. II permits us to neatly fit the data at all temperatures.

The temperature dependence of the stickiness parameter $\tau$ for microemulsions with different molar water/AOT ratio is illustrated in Fig. 8. In general, the strength of the attractive potential between the droplets yielded by the fitting procedure is self-consistent; that is, the potential increases at constant $w_o$ with increasing temperature and at constant temperature with decreasing $w_o$. The systems with higher $w_o$ values (45 and 56) yield $\tau=100$ at the hard-sphere limit. The $w_o=35$ system displays the hard-sphere behavior at low temperatures, but the stickiness increases (i.e., $\tau$ decreases) with increasing temperature. At $w_o=25$, the stickiness increases further so that the droplets display attractive behavior even at lower temperatures. Note that the interactions of the droplets at low $w_o$ values change drastically from hard-sphere behavior to strong attraction at temperatures much below the onset of cylinder formation. At $w_o=25$, for ex-

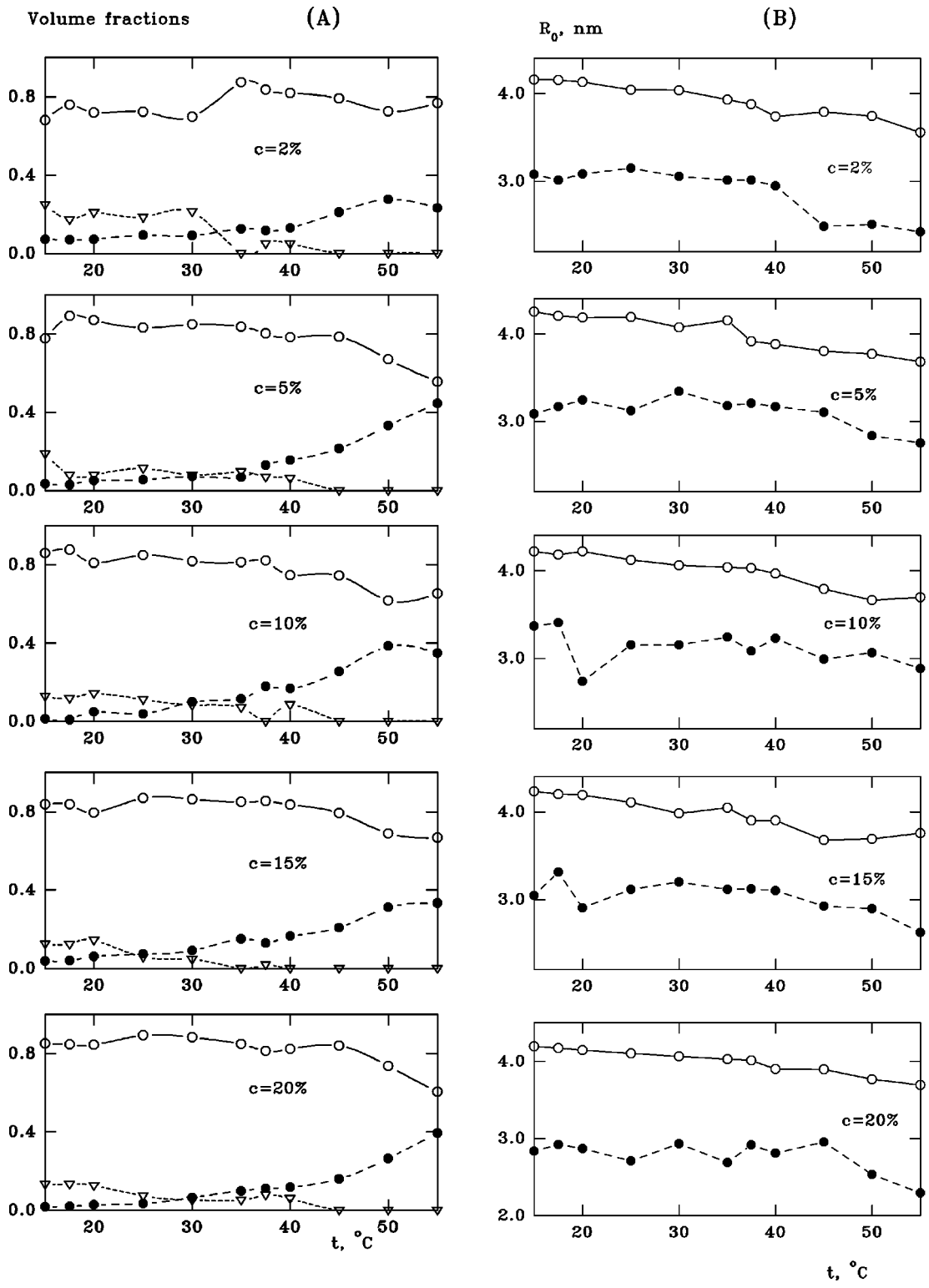


FIG. 5. Structural parameters as functions of temperature for different droplet concentrations (from $c_w = 2\%$ to 20%) in the AOT–water–iso-octane microemulsion system at $w_o = 25$. (A) Relative volume fractions of components, (B) Average radii of water droplets and cylindrical aggregates. Open circles: microemulsion droplets; filled circles: cylinders; triangles: AOT reverse micelles. The propagated errors do not exceed the symbol size.

ample, $\log(\tau)$ already approaches zero at 25 °C, whereas cylinders only start to form above 40 °C [see Fig. 5(a), bottom].

### D. Influence of salt

The scattering curves from the AOT–water–decane microemulsions (salt-free and with added NaCl) were analyzed as described above for the iso-octane systems. Decane was used instead of iso-octane for the study of the salt dependence because addition of salt shifts the existence region to higher temperatures, whereas the decane system lies about 15 °C lower in temperature than the iso-octane system. Figure 9 presents the fitted scattering curves for the decane sys-

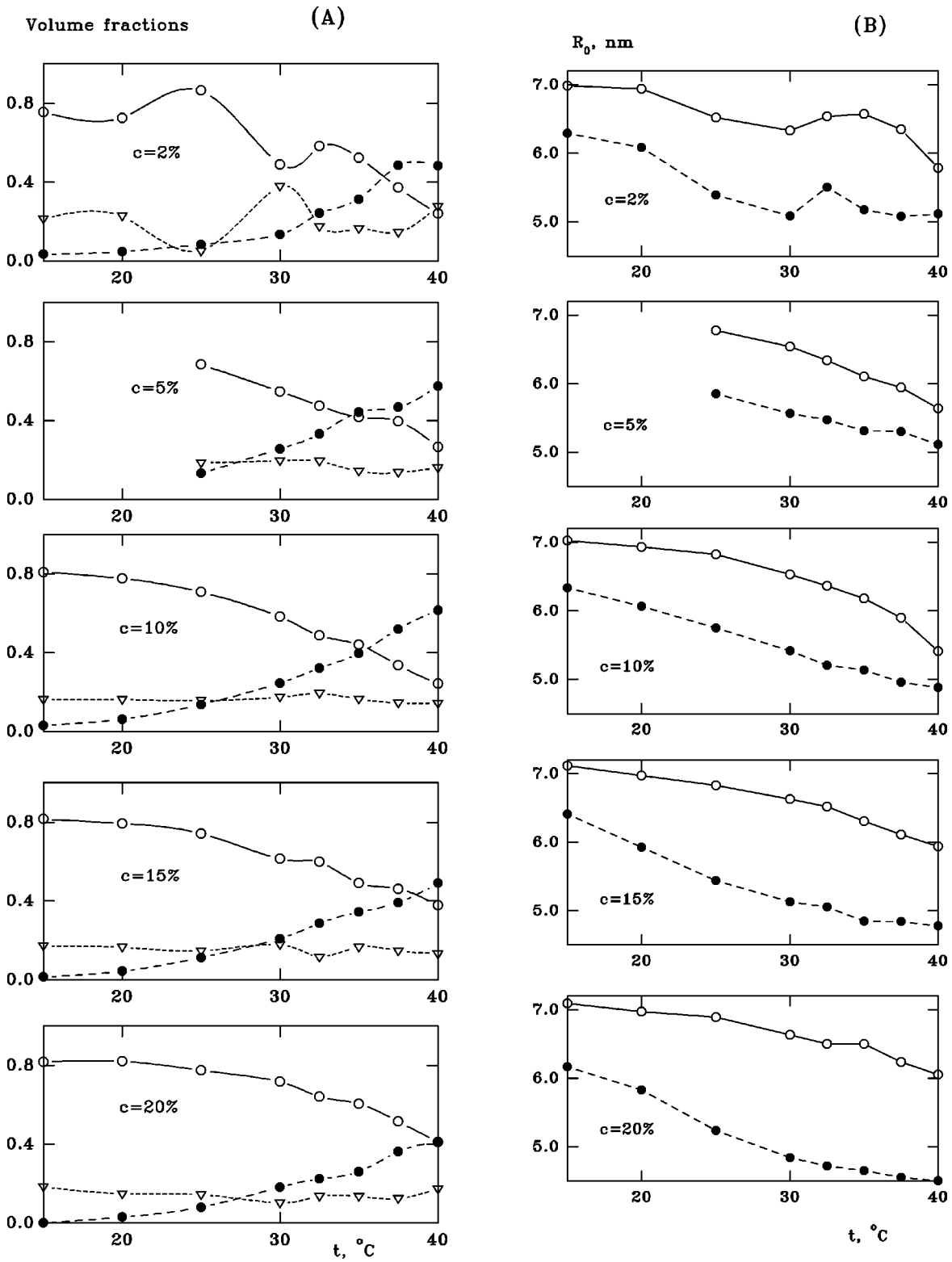


FIG. 6. Structural parameters as functions of temperature for different droplet concentrations in the AOT–water–iso-octane microemulsion system $w_o = 45$. Notations are as in Fig. 5.

tems ($w_o = 36.8$ and 50.3 at $c_w = 10\%$) at a temperature of 35 °C with salt concentrations ranging from $\varepsilon = 0\%$ to 0.6%. For all data sets, the microemulsion samples have been measured up to the upper phase boundary. Addition of salt clearly induces noticeable changes in the scattering curves. The scattering curves in Fig. 9 suggest that the samples at $\varepsilon = 0.2\%$ contain more cylindrical aggregates than the others. Quantitative results are given in Fig. 10, presenting the volume fractions and the average radii of the cylindrical aggregates as functions of temperature for the two systems at different salt concentrations. Formation of cylinders is maximal at $\varepsilon = 0.2\%$, but further increase of the NaCl concentration

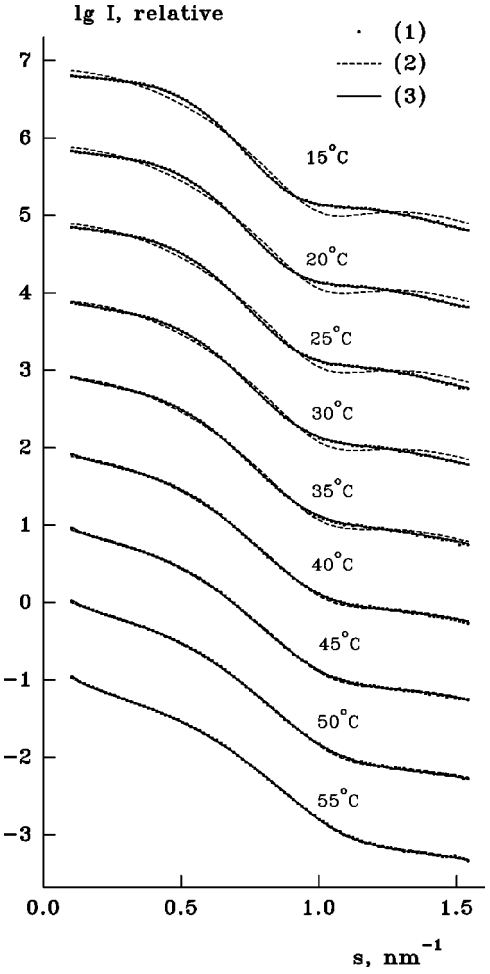


FIG. 7. Fits of the scattering data from the AOT–water–iso-octane microemulsions at $w_o=25$, $c_w=20\%$. (1): Experimental data; (2) and (3): Best fits provided by the three-component model without and with accounting for interference effects, respectively. Successive curves in each plot are displaced as in Fig. 2.

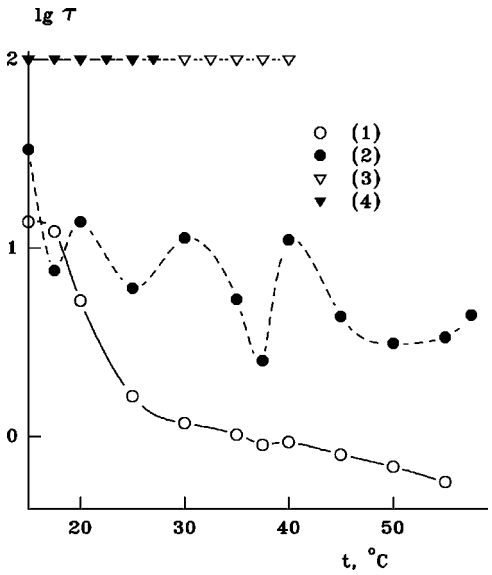


FIG. 8. Stickiness of the water droplets as a function of temperature for AOT systems at a droplet concentration $c_w=20\%$. Curves (1–4) correspond to $w_o=25$, 35, 45, and 56, respectively.

reduces the fraction of cylinders. For $w_o=36.8$, a volume fraction of cylinders above 80% is found close to the upper phase boundary. At $\varepsilon=0.6\%$, the system with $w_o=36.8$ contains rather thin cylinders with radii ranging from 40 to 30 Å. The microemulsions at $w_o=50.3$ yield rather consistent trends of the cylinder volume fractions and radii at the different salt concentrations.

## V. DISCUSSION

The approach developed above to analyze the scattering data on structural transitions in the $L_2$ phase of AOT microemulsions can also be used to characterize other polydisperse mixtures. A prerequisite for such nonlinear modeling is an appropriate selection of the parameters describing the system, which is only possible if extensive *a priori* information is available (as for AOT microemulsions). The three components describing the droplet-to-cylinder transition of the AOT microemulsions yield distinctly different contribution to the total intensity (see the example in Fig. 11), and this makes it possible to reliably decompose the experimental data into the scattering from the components. According to Shannon's sampling theorem[71,72] the number of independent parameters required to describe a scattering curve is $N_s=s_{\max}D_{\max}/\pi$, where $D_{\max}$ is the maximum particle size in the system [see Eq. (13)]. Calculations using the indirect transformation program GNOM indicate that $D_{\max}$ is at least 50 nm ($N_s=25$) for most data sets and in all cases exceeds 30 nm ($N_s=14$). Our fitting procedure, using seven free parameters only, is thus fully justified by the information content in the scattering data. Nevertheless, a clear distinction must be made between the parameters that can be meaningfully adjusted in the fitting process and those that produce only marginal changes in the calculated curves. The latter parameters should be fixed to avoid deteriorating the nonlinear minimization process. In the present study, the radius of the AOT reversed micelles $R_3$, the cylinder length $L$, and the effective width of the AOT tails $d_t$ were fixed because the scattering curves were not sufficiently sensitive to variations of these parameters to justify their optimization.

It should be noted that the volume fractions of the small particles found (presumably, AOT inverse micelles) depend strongly on the outer part of the scattering patterns and are thus sensitive to background subtraction. The presence of the inverse micelles is clearly required to fit the numerous scattering data sets analyzed in the present study. Additional scattering experiments in a wider angular range are required to further confirm the existence of the inverse micelles and to characterize their volume fractions more reliably.

In the present paper, the interference effects were taken in a simplified form assuming the scattering to be a product of the average form factor and structure factor. To check the validity of this approximation, calculated scattering curves were compared to those computed using the analytical scattering function,[73] and only marginal differences were found up to polydispersities of 50%. This justifies the use of Eq. (7), permitting a rapid computation of the theoretical scattering intensities and thus accelerates the nonlinear minimization process significantly. An attempt to account for the in-

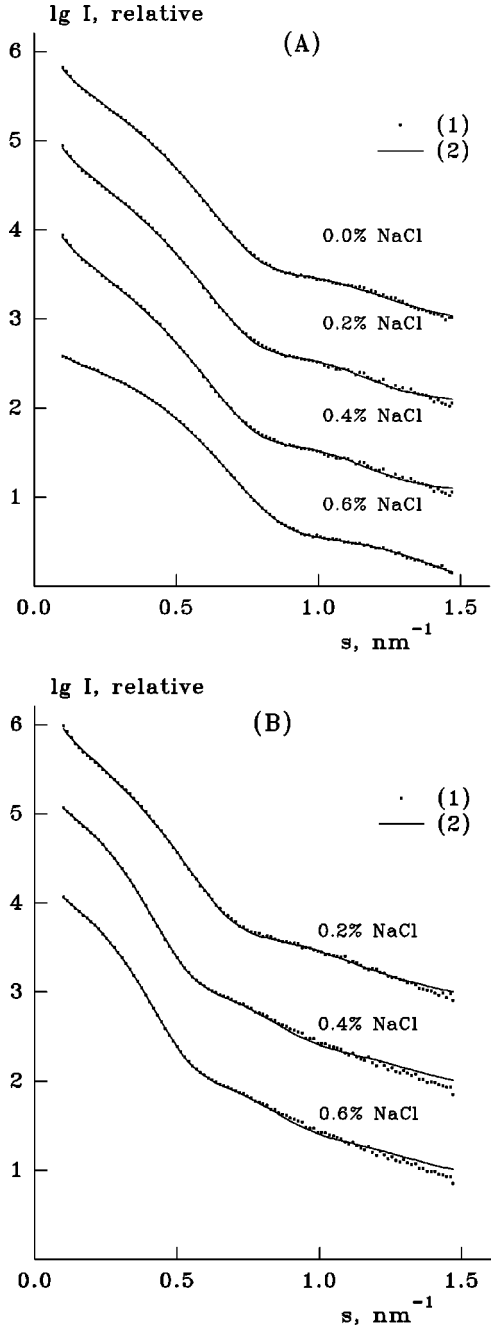


FIG. 9. Fits of the scattering data from the AOT–water–decane microemulsions at a droplet concentration $c_w = 10\%$ and temperature of $t = 35\,^{\circ}\mathrm{C}$ for different salt concentrations in the aqueous phase. Panels (A) and (B) correspond to $w_o = 36.76$, and 50.32, respectively. (1): Experimental data; (2): The fits provided by the three-component model with interactions. Successive curves in each plot are displaced as in Fig. 2.

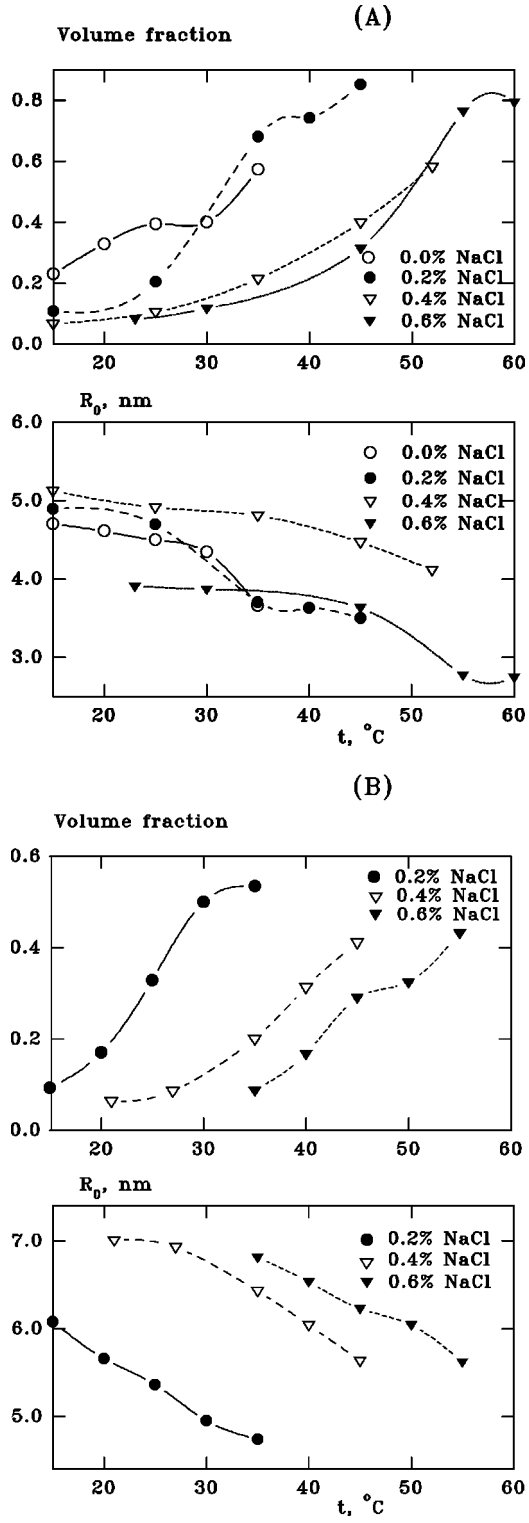


FIG. 10. Relative volume fractions of cylinders and their average radii as functions of temperature for the AOT–water–decane microemulsions at a droplet concentration $c_w = 10\%$. Panels (A) and (B) correspond to $w_o = 36.8$ and 50.32, respectively, showing curves for different salt concentrations of 0.0%, 0.2%, 0.4%, and 0.6% NaCl. The propagated errors do not exceed the symbol size.

terference between the cylinders using the formulas derived in Refs. 74 and 75 did not yield any significant changes in the results. At higher temperatures the volume fraction of cylinders grew by up to 10%, but the fits to the experimental data were better if the interference between the cylinders was omitted.

It should be stressed that the changes in the scattering patterns with increasing temperature cannot be satisfactorily explained by aggregation of the spherical droplets only. Figure 12 illustrates the fits obtained at the highest temperatures and highest water concentrations ($\varphi_w = 20\%$) for different $w_o$-values with $\varphi_2$ fixed at zero, i.e., without introducing the cylindrical particles but still accounting for the attractive potential between the spheres. Despite the fact that in all cases

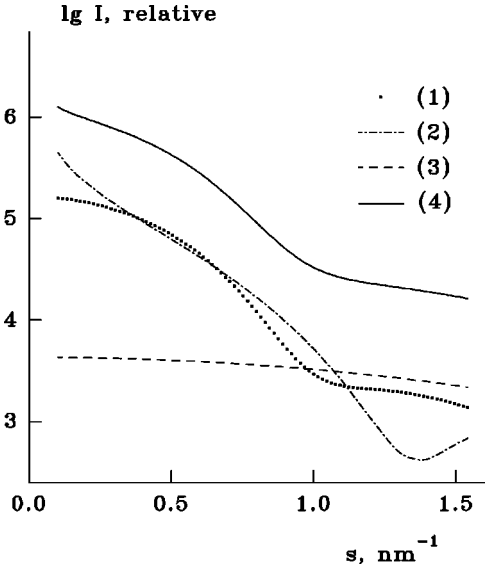


FIG. 11. Partial scattering intensities from the three components for the best fit of the scattering curve from the sample with $c_w=5\%$, $w_o=35$, and $T=55\,^{\circ}\mathrm{C}$. (1): Spherical droplets; (2) Cylinders; and (3): Reversed AOT micelles; (4): Weighted sum of the three partial intensities. The latter curve is displaced upwards by one logarithmic unit for better visualization.

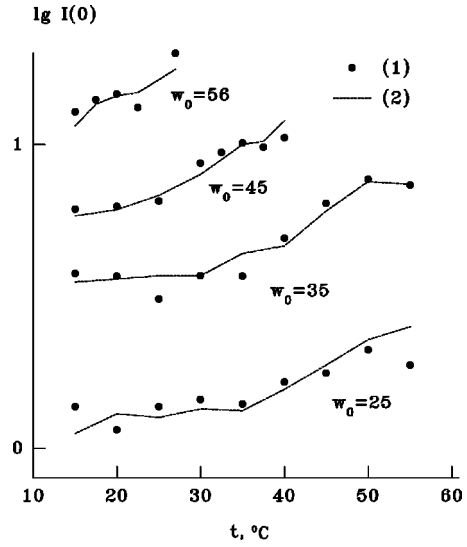


FIG. 13. Experimental (1) and predicted (2) values of the forward scattering as functions of temperature for the AOT–water–iso-octane microemulsions at $c_w=5\%$ and $w_o=25$, 35, 45, and 56. For each $w_o$, the predicted values are multiplied by a scale factor to best fit the dependence observed for the experimental values.

the stickiness parameter of the spherical droplets was about $\tau=0.2$ (near the limit of the maximum possible attraction within the sticky hard-sphere model[57]), these fits display clear systematic deviations from the experimental data and the value of the residual $\chi$ is three to seven times larger than that provided by the three-component fitting. It is interesting that the systematic deviations are not restricted to the initial part of the scattering pattern but occur over the entire range of the momentum transfer.

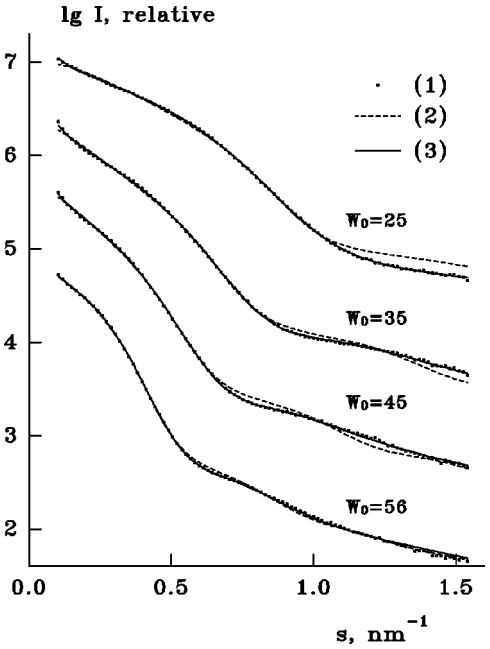


FIG. 12. Fits of the scattering data from the AOT–water–iso-octane microemulsions at $c_w=20\%$ (C) and $w_o=25$, 35, 45, and 56. (1): Experimental data; (2) and (3): Best fits provided by the two-component model without the cylinders but with attractive interactions between the droplets, and by the three-component model, respectively. For each $w_o$, the results at the highest temperature are presented. Successive curves are displaced downwards by one logarithmic unit for better visualization.

The quality of the fit to the experimental data is perhaps astonishing, given that the interactions between cylinders and between cylinders and droplets were neglected. Even for very anisometric particles like cylinders, the shape of the structure factor is, however, mainly defined by the center-to-center distance between particles.[76] Moreover, except at the lowest momentum transfer values, the scattering of the cylinders is effectively that of the cross section, which has a diameter similar to that of the droplets. It is possible that the structure factor of the droplets would also contain contributions from other types of interactions and that this would contribute to the good fit.

The determination of relative volume fractions of components in a mixture depends only on the geometry of the scattering curve, and does not require measurements on an absolute scale. The results can, however, be verified against the values of the forward scattering $I(0)$ obtained by extrapolation of the experimental data normalized as described in Sec. III B. Figure 13 presents the values of $I(0)$ computed from Eq. (4) along with those evaluated from the experimental data by the indirect Fourier transformation method for $c=5\%$ and different $w_o$. The experimental forward scattering displays the same temperature trend as the values predicted by Eq. (4), although the latter were obtained by fitting the data on a relative scale. Similar agreement was observed for other temperature series.

The simplified model used in this study allowed us to accurately fit numerous experimental data sets recorded in different conditions, which demonstrates the effectiveness of the method for quantitative characterization of polydisperse mixtures. Further analysis of the entire set of scattering data of the AOT microemulsions is now in progress, but from the above results it is already clear that it is possible to extract

characteristics of the different structures formed within the $L_2$-phase region of the AOT microemulsions. Not only could changes in the volume fractions with increasing temperature or salt concentration be monitored, but it was also possible to detect concomitant variations in the radii of the microemulsion droplets and cylinders. Both radii decrease with increasing temperature, with the ratio between the radius of the cylinders and the droplets between 0.7–0.8. From simple geometrical considerations, it follows that if all spheres would transform into cylinders the cylinder/droplet radii ratio should be equal to 0.67. This value was indeed approached if one takes, in one temperature series at a given $w_o$ and $c_w$, the value of the droplet radius at the lowest temperature and that from the cylinder at the highest temperature. It is certainly also an important result in that it seems to be possible to study droplet interactions independently of the formation of cylinders. Our results indicate that spherical droplets are still present in significant amounts at the upper temperature limits of the phases, and that the cylindrical aggregates are already significantly elongated when they start to appear. The large experimental data set provides a solid base, allowing us to further discuss the results on droplet–cylinder transitions within the concept of the curvature energy and to compare them with the findings on droplet aggregation and channel formation obtained by other techniques.

## ACKNOWLEDGMENTS

The authors acknowledge the financial support provided by the INTAS (International Association for the Promotion of Cooperation with Scientists from New Independent States of the former Soviet Union) Grant No 96-1115. This work has been supported by the Netherlands Foundation for Chemical Research (NWO-CW) in collaboration with the Netherlands Technology Foundation (STW).

[1] D. F. Evans and H. Wennerström, *The Colloidal Domain: Where Physics, Chemistry, Biology and Technology Meet*, 2nd ed. (Wiley-CH, New York, 1999).
[2] H. T. Davis, J. F. Bodet, L. E. Scriven, and W. G. Miller in *Physics of Amphiphilic Layers*, edited by J. Meunier, D. Langevin, and N. Boccara (Springer, Berlin, 1987), pp. 310–327.
[3] M. Kahlweit, R. Strey, and G. Busse, J. Phys. Chem. **94**, 3881 (1990).
[4] Y. Chevalier and T. Zemb, Rep. Prog. Phys. **53**, 279 (1990).
[5] J. Eastoe, B. H. Robinson, D. C. Steytler, and D. Thorn-Leeson, Adv. Colloid Interface Sci. **36**, 1 (1991).
[6] U. Olsson and H. Wennerström, Adv. Colloid Interface Sci. **49**, 113 (1994).
[7] W. Helfrich, Z. Naturforsch. C **28**, 693 (1973).
[8] P. G. de Gennes and C. Taupin, J. Phys. Chem. **86**, 2294 (1982).
[9] *Micelles, Membranes, Microemulsions, and Monolayers*, edited by W. M. Gelbart, A. Ben-Shaul, and D. Roux (Springer, New York, 1994).
[10] S. A. Safran, *Statistical Thermodynamics of Surfaces, Interfaces, and Membranes* (Adison-Wesley, Reading, MA, 1994).
[11] G. J. M. Koper, W. F. C. Sager, J. Smeets, and D. Bedeaux, J. Phys. Chem. **99**, 13291 (1995).
[12] D. Chatenay, W. Urbach, A. M. Cazabat, and D. Langevin, Phys. Rev. Lett. **54**, 2253 (1985).
[13] R. Johannsson, M. Almgren, and J. Alsins, J. Phys. Chem. **95**, 3819 (1991).
[14] P. D. I. Fletcher and J. S. Morris, Colloids Surf., A **98**, 147 (1995).
[15] S. Bhattacharya, J. P. Stokes, M. W. Kim, and J. S. Huang, Phys. Rev. Lett. **55**, 1884 (1985).
[16] C. Cametti, P. Codastefano, P. Tartaglia, S.-H. Chen, and J. Rouch, Phys. Rev. A **45**, R5358 (1992).
[17] W. Sager, W. Sun, and H.-F. Eicke, Prog. Colloid Polym. Sci. **89**, 284 (1992).
[18] L. Schlicht, J. H. Spilgies, F. Runge, S. Lipgens, S. Boye, D. Schübel, and G. Ilgenfritz, Biophys. Chem. **58**, 39 (1996).
[19] L. M. M. Nazario, T. A. Hatton, and J. P. S. G. Crespo, Langmuir **12**, 6326 (1996).
[20] S.-H. Chen, S.-L. Chang, and R. Strey, J. Chem. Phys. **93**, 1907 (1990).
[21] J. S. Huang and M. W. Kim, Phys. Rev. Lett. **47**, 1462 (1981).
[22] B. H. Robinson, C. Toprakcioglu, J. C. Dore, and P. Chieux, J. Chem. Soc., Faraday Trans. 1 **80**, 13 (1984).
[23] M. Kotlarchyk, R. B. Stephens, and J. S. Huang, J. Phys. Chem. **92**, 1533 (1988).
[24] R. Hilfiker, H.-F. Eicke, W. Sager, C. Steeb, U. Hofmeier, and R. Gehrke, Ber. Bunsenges. Phys. Chem. **94**, 677 (1990).
[25] M. Kotlarchyk, J. S. Huang, and S.-H. Chen, J. Phys. Chem. **89**, 4382 (1985).
[26] M. Kotlarchyk, S.-H. Chen, and J. S. Huang, J. Phys. Chem. **86**, 3273 (1982).
[27] C. Robertus, W. H. Philipse, J. G. H. Joosten, and Y. K. Levine, J. Chem. Phys. **90**, 4482 (1989).
[28] C. Robertus, J. G. H. Joosten, and Y. K. Levine, J. Chem. Phys. **93**, 7293 (1990).
[29] S. H. Chen, C. Y. Ku, J. Rouch, P. Tartaglia, C. Cametti, and J. Samseth, J. Phys. IV **3**, 143 (1993).
[30] W. F. C. Sager and E. M. Blokhuis, Prog. Colloid Polym. Sci. **110**, 258 (1998).
[31] E. M. Blokhuis and W. F. C. Sager, J. Chem. Phys. **110**, 3148 (1999).
[32] E. M. Blokhuis and W. F. C. Sager, J. Chem. Phys. **111**, 7062 (1999).
[33] M. Kotlarchyk, S.-H. Chen, and J. S. Huang, Phys. Rev. A **28**, 508 (1983).
[34] L. J. Magid, R. Triolo, and J. S. Johnson, Jr., J. Chem. Phys. **81**, 5161 (1984).
[35] M. Kotlarchyk, S.-H. Chen, J. S. Huang, and M. W. Kim, Phys. Rev. A **29**, 2054 (1984).
[36] S. Lipgens, D. Schübel, L. Schlicht, J.-H. Spilgies, G. Ilgenfritz, J. Eastoe, and R. K. Heenan, Langmuir **14**, 1041 (1998).
[37] J. Eatoe, G. Fragneto, B. H. Robinson, T. F. Towey, R. K. Heenan, and F. J. Leng, J. Chem. Soc., Faraday Trans. **88**(3), 461 (1992).
[38] E. Bardez, N. Cao Vy, and Th. Zemb, Langmuir **11**, 3374 (1995).
[39] J. Tanori, T. Gulik-Krzywicki, and M. P. Pileni, Langmuir **13**, 632 (1997).
[40] O. Glatter, R. Strey, K.-V. Schubert, and E. W. Kaler, Ber. Bunsenges. Phys. Chem. **100**, 323 (1996).
[41] J. Brunner-Popela, R. Mittelbach, R. Strey, K.-V. Schubert, E. W. Kaler, and O. Glatter, J. Chem. Phys. **110**, 10623 (1999).
[42] M. Teubner and R. Strey, J. Chem. Phys. **87**, 3195 (1987).
[43] B. W. Ninham, I. S. Barnes, S. T. Hyde, P. J. Derian, and T. N. Zemb, Europhys. Lett. **4**(5), 561 (1987).
[44] M. S. Leaver, U. Olsson, H. Wennerström, and R. Strey, J. Phys. II **4**, 515 (1994).
[45] W. F. C. Sager, Langmuir **14**, 6385 (1998).
[46] J. S. Huang, S. T. Milner, B. Farago, and D. Richter, Phys. Rev. Lett. **59**, 2600 (1987).
[47] M. Borkovec and H.-F. Eicke, Chem. Phys. Lett. **157**, 457 (1989).
[48] E. van der Linden, D. Bedeaux, and M. Borkovec, Physica A **162**, 99 (1989).
[49] B. Farago, in *Structure of Dynamics of Strongly Interacting Colloids and Supramolecular Aggregates in Solution*, edited by S.-H. Chen, J. S. Huang, and P. Tartaglia (Kluwer, Dordrecht, 1992), pp. 365–373.
[50] B. P. Binks, H. Kellay, and J. Meunier, Europhys. Lett. **16**, 53 (1991).
[51] H. Kellay, J. Meunier, and B. P. Binks, Phys. Rev. Lett. **70**, 1485 (1993).
[52] H. Kellay, B. P. Binks, Y. Hendrikx, L. T. Lee, and J. Meunier, Adv. Colloid Interface Sci. **49**, 85 (1994).
[53] S. Koenig, D. I. Svergun, M. H. J. Koch, G. Huebner, and A. Schellenberger, Biochemistry **31**, 8726 (1992).
[54] G. V. Schulz, Z. Phys. Chem. Abt. B **30**, 379 (1935).
[55] L. A. Feigin and D. L. Svergun, in *Structure Analysis by Small-Angle X-ray and Neutron Scattering*, edited by G. W. Taylor (Plenum, New York, 1987), p. 92.
[56] J. K. Percus and G. J. Yevick, Phys. Rev. **110**, 1 (1958).
[57] R. J. Baxter, J. Chem. Phys. **49**, 2270 (1968).
[58] *Practical Optimisation*, edited by P. E. Gill, W. Murray, and M. H. Wright (Academic, London, 1981).

[59] J. Smeets, G. J. M. Koper, J. P. M. van der Ploeg, and D. Bedeaux, Langmuir **10**, 1387 (1994).
[60] M. H. J. Koch and J. Bordas, Nucl. Instrum. Methods **208**, 461 (1983).
[61] C. J. Boulin, R. Kempf, M. H. J. Koch, and S. M. McLaughlin, Nucl. Instrum. Methods Phys. Res. A **249**, 399 (1986).
[62] C. J. Boulin, R. Kempf, A. Gabriel, and M. H. J. Koch, Nucl. Instrum. Methods Phys. Res. A **269**, 312 (1988).
[63] A. Gabriel and F. Dauvergne, Nucl. Instrum. Methods **201**, 223 (1982).
[64] A. M. Petrascu, M. H. J. Koch, and A. Gabriel, J. Macromol. Sci., Phys. **B37(4)**, 463 (1998).
[65] D. I. Svergun, A. V. Semenyuk, and L. A. Feigin, Acta Crystallogr., Sect. A: Found. Crystallogr. **A44**, 244 (1988).
[66] D. I. Svergun, J. Appl. Crystallogr. **25**, 495 (1992).
[67] A. N. North, J. C. Dore, J. A. McDonald, B. H. Robinson, R. K. Heenan, and A. M. Howe, Colloids Surface **19**, 21 (1986).
[68] J. N. Israelachvili, D. J. Mitchell, and B. W. Ninham, J. Chem. Soc., Faraday Trans. 2 **72**, 1525 (1976).
[69] M. E. Cates and S. J. Candau, J. Phys.: Condens. Matter **2**, 6869 (1990).
[70] R. Menes, S. A. Safran, and R. Strey, Phys. Rev. Lett. **74**, 3399 (1995).
[71] C. E. Shannon and W. Weaver, *The Mathematical Theory of Communication* (University of Illinois Press, Urbana, 1949).
[72] P. B. Moore, J. Appl. Crystallogr. **13**, 168 (1980).
[73] W. L. Griffith, R. Triolo, and A. L. Compere, Phys. Rev. A **35**, 2200 (1987).
[74] T. Shimada, M. Doi, and K. Okano, J. Chem. Phys. **88**, 2815 (1988).
[75] P. van der Schoot, Macromolecules **25**, 2923 (1992).
[76] B. Weyerich, B. D'Aguanno, E. Canessa, and R. Klein, Proc. Faraday Discuss. Chem. **90**, 245 (1990).